Dalton Transactions

PAPER

View Article Online
View Journal | View Issue

Cite this: *Dalton Trans.*, 2014, **43**, 9283

Seed-mediated synthesis of bimetallic ruthenium–platinum nanoparticles efficient in cinnamaldehyde selective hydrogenation†

Xueqiang Qi,[a,b] M. Rosa Axet,*[a,b] Karine Philippot,*[b,c] Pierre Lecante[d,e] and Philippe Serp[a,b]

Received 17th December 2013,
Accepted 10th April 2014

DOI: 10.1039/c3dt53539h

www.rsc.org/dalton

Core–shell RuPt (Ru core–Pt shell) and PtRu (Pt core–Ru shell) nanoparticles were prepared by decomposing in a two-step procedure a ruthenium ([Ru(COD)(COT)] (COD = 1,5-cyclooctadiene, COT = 1,3,5-cyclooctatriene)) and a platinum complex ($[Pt_2(dba)_3]$ (dba = dibenzylideneacetone) or $[Pt(CH_3)_2(COD)]$) in the presence of 4-(3-phenylpropyl)pyridine (PPP) as a stabilizer and using different Ru/Pt ratios. The data obtained from a combination of several analyses (TEM, HRTEM, WAXS and IR) indicate that the so-obtained nanoparticles present a core–shell structure. The catalytic performances of these bimetallic nanoparticles for the selective hydrogenation of *trans*-cinnamaldehyde were investigated, which provided interesting results as well as useful information to elucidate their structure and composition. Indeed, the catalytic results evidence that: (1) the combination of both metals led in some cases to a synergistic effect on the selectivity of the reaction, and (2) the structure and the composition affected the selectivity of the reaction.

Introduction

There has been for some years growing interest in the synthesis of structure-controlled metal nanoparticles (NPs) for application in catalysis.[1] More specifically, the higher activity and selectivity of bimetallic NPs compared to those of the monometallic ones are typically attributed to ensemble and/or ligand (electronic) effects.[2] Bimetallic RuPt NPs are mainly used in catalysis for methanol[3,4] and ethanol[5] electrooxidation in fuel cells, for CO preferential oxidation[6] and for selective hydrogenation.[7–9] In all cases, control over the shape and chemical order is crucial, since it will impact NP properties.[1] Although the control over the chemical order is well documented for large NPs (>5 nm), for the smaller ones, it is much more difficult to achieve.[10] For selective hydrogenation, it was found that the composition and structure of NPs (surface ligands, size, shape, and chemical order) affect the catalytic performances.[11] Therefore the analysis of the catalysis results can be used as complementary information for characterizing bimetallic NPs.

Some of us have developed mild synthetic techniques to prepare in solution metal NPs from coordination compounds.[12] In this way, NPs of well-dispersed and well-controlled size can be obtained using surface stabilizing ligands.[13,14] This "chimie douce" method is also suitable for synthesizing bimetallic NPs with specific structural composition.[15] In the case of bimetallic RuPt NPs, alloy,[16] core–shell,[17] and NPs displaying a Ru rich core and a disordered shell containing both Ru and Pt[18] have been successfully prepared.[17,18] RuPt alloy NPs were obtained by co-decomposition of [Ru(COD)(COT)] and $[Pt_2(dba)_3]$ in the presence of PVP (polyvinylpyrrolidone). Changing the platinum precursor $[Pt_2(dba)_3]$ for $[Pt(CH_3)_2(COD)]$ led to the formation of core–shell NPs, as $[Pt(CH_3)_2(COD)]$ is decomposed at a slower rate. The chemical segregation to obtain core–shell RuPt NPs resulted from kinetics (decomposition time) and thermodynamics (preferred location in the particle) parameters of the two metal precursors. The use of a coordinating ligand (dppb, diphenylphosphinobutane) instead of PVP, which is a steric stabilizer inert to the metals, strongly affected the structure of RuPt NPs. Thus, the co-decomposition of [Ru(COD)(COT)] and $[Pt(CH_3)_2(COD)]$ in the presence of dppb led to NPs displaying a Ru rich core and a disordered shell containing both Ru and Pt, instead of an alloy or a core–shell structure.

[a]*CNRS, LCC (Laboratoire de Chimie de Coordination), Composante ENSIACET, 4 allée Emile Monso, BP 44099, F-31030 Toulouse Cedex 4, France*
[b]*Université de Toulouse, UPS, INPT, F-31077 Toulouse Cedex 4, France. E-mail: rosa.axet@lcc-toulouse.fr, karine.philippot@lcc-toulouse.fr; http://www.lcc-toulouse.fr*
[c]*CNRS, LCC (Laboratoire de Chimie de Coordination), 205 route de Narbonne, BP 44099, F-31077 Toulouse Cedex 4, France*
[d]*CNRS; CEMES (Centre d'Elaboration de Matériaux et d'Etudes Structurales), BP 94347, 29 rue Jeanne Marvig, F-31055 Toulouse, France*
[e]*Université de Toulouse; UPS, F-31055 Toulouse, France*
†Electronic supplementary information (ESI) available. See DOI: 10.1039/c3dt53539h

With the aim to synthesise core–shell NPs in the presence of a coordinating ligand we propose here a two-step procedure instead of co-decomposition. In this way, preformed monometallic NPs are used as seeds for a second decomposition step. As precursors, we chose [Ru(COD)(COT)] and [Pt(CH$_3$)$_2$(COD)] to synthesize **RuPt** NPs (Ru core–Pt shell), and [Pt$_2$(dba)$_3$] and [Ru(COD)(COT)] to synthesize **PtRu** NPs (Pt core–Ru shell). The NPs were synthesised in the presence of 4-(3-phenylpropyl)pyridine (PPP) since it is an excellent stabilizer for metal NPs, as demonstrated for Pd,[19,20] Ru[20–23] and RuPt.[8,9] As shown for Ru NPs, PPP strongly interacts with the metal surface through π-interactions acting as a "bidentate" ligand even under hydrogenation conditions. In addition, we also report the catalytic performances of these bimetallic nanocatalysts for the selective hydrogenation of cinnamaldehyde. The selectivity of the hydrogenation of α,β-unsaturated aldehydes depends on several factors, such as the nature of the metal, the size of metal particles, and the presence of a second metal.[24–26] The catalytic results provide additional information on the catalyst structure and help us to elucidate the surface composition of the reported nanoparticles.

Results and discussion

Synthesis of metal nanoparticles

The core–shell bimetallic NPs were synthesised by decomposing in a two-step procedure a ruthenium complex ([Ru(COD)(COT)] (COD = 1,5-cyclooctadiene, COT = 1,3,5-cyclooctatriene)) and a platinum complex ([Pt$_2$(dba)$_3$] (dba = dibenzylideneacetone) or [Pt(CH$_3$)$_2$(COD)]) in the presence of 4-(3-phenylpropyl)-pyridine (PPP) as a stabilizer. In both cases (**RuPt** and **PtRu**) the aim was to evaluate the effect of the thickness of the outer layer on the characteristics of the nanocatalysts. We have roughly estimated the minimum number of atoms needed to achieve a complete monolayer around the preformed metal cores and chosen different metal–metal ratios to vary the thickness of the outer shell (see ESI.1†). For both kinds of core–shell NPs (**RuPt** or **PtRu**) we thus assumed an ideal sphere of 83 atoms for the core (a diameter of 1.5 nm for Ru and 1.6 nm for Pt, which are relatively close to the experimental values, see below). A molar ratio of 1 : 2 is needed to form a complete second metal monolayer (a ratio 1 : 1 gives roughly half a monolayer), and a 1 : 4 metal ratio leads to almost two monolayers.

The first series of NPs, namely **RuPt** (Ru core–Pt shell), was prepared by decomposing in the first step [Ru(COD)(COT)] under 3 bar of H_2 at room temperature (r.t.) in THF (tetrahydrofuran) and in the presence of PPP as a stabilizing ligand. Then, [Pt(CH$_3$)$_2$(COD)] and additional PPP were added to the colloidal solution containing preformed Ru seeds to further react at 70 °C under 3 bar H_2. Three samples using three different metal molar ratios were prepared following these conditions: **Ru1Pt1** using one molar equivalent of each metal, **Ru1Pt2** using 2 equivalents of platinum with respect to ruthenium, and finally **Ru1Pt4** using 4 equivalents of platinum with respect to ruthenium (Scheme 1). The second series of NPs, namely **PtRu** (Pt core–Ru shell), was obtained by decomposing in the first step [Pt$_2$(dba)$_3$] under 1 bar of CO at r.t. and then [Ru(COD)(COT)] and PPP were added to the colloidal suspension and decomposed at r.t. under 3 bar of H_2. The [Pt(CH$_3$)$_2$(COD)]/PPP system was not used for this series since its decomposition under dihydrogen produces very large Pt particles (see ESI.2†). Three samples were synthesized in that way: **Pt1Ru1**, **Pt1Ru2** and **Pt1Ru4** (Pt–Ru 1 : 1, 1 : 2 and 1 : 4, respectively, see Scheme 2). Furthermore, as a reference system, we also prepared alloyed bimetallic NPs **Pt@Ru** by co-decomposition of [Ru(COD)(COT)] and [Pt(CH$_3$)$_2$(COD)] in the presence of PPP, as previously reported by some of us.[9] For comparative purposes, monometallic ruthenium and platinum NPs (**Ru/PPP**,[21] **Pt/PPP** and **Pt/CO**[27]) were also synthesized from [Ru(COD)(COT)]/PPP, [Pt(CH$_3$)$_2$(COD)]/PPP and [Pt$_2$(dba)$_3$]/CO, respectively.

The size and the structure of the NPs were analysed by TEM (transmission electron microscopy), HRTEM (high resolution transmission electron microscopy) and WAXS (wide-angle X-ray scattering). The adsorption of carbon monoxide on the NP surface was also investigated by infrared spectroscopy in the solid state.

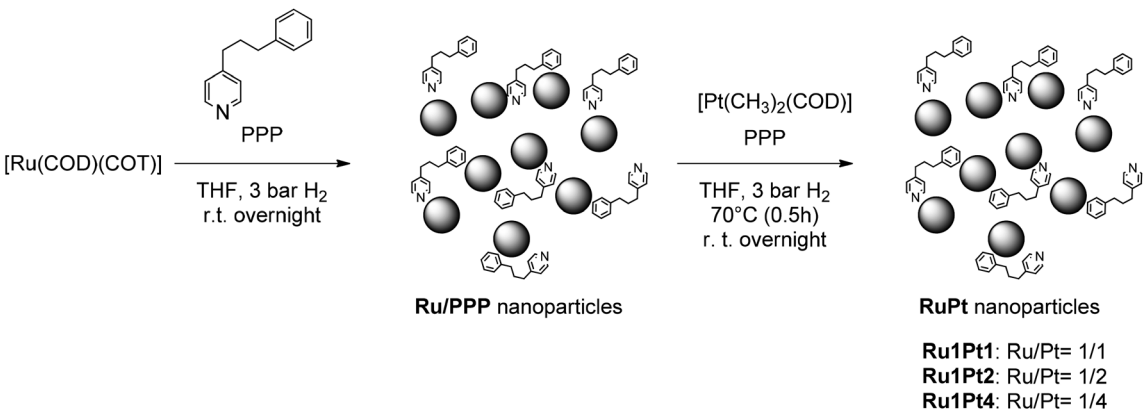

Scheme 1 Synthesis of the **RuPt** NPs.

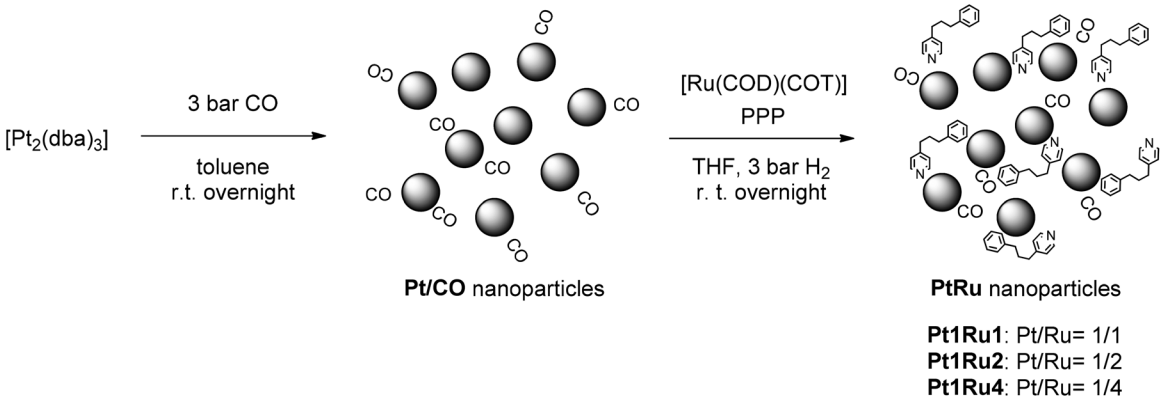

Scheme 2 Synthesis of the **PtRu** NPs.

TEM, HRTEM and WAXS analyses

The TEM analyses of the **RuPt** series (**Ru1Pt1**, **Ru1Pt2** and **Ru1Pt4**) show crystalline and monodisperse NPs with a mean size of *ca.* 1.8 nm for all the samples: *ca.* 1.8 (0.5) nm for **Ru1Pt1**, *ca.* 1.8 (0.4) nm for **Ru1Pt2** and *ca.* 1.8 (0.5) nm for **Ru1Pt4** (see Fig. 1). Since the monometallic ruthenium NPs (**Ru/PPP**) resulting from the first step display a mean size of *ca.* 1.4 (0.2) nm (Fig. 1-d), the higher mean size observed for the RuPt NPs indicates that the decomposition of $[Pt(CH_3)_2(COD)]$ during the second step takes place on the surface of **Ru/PPP**, thus leading to an increase of the mean size (in agreement with our estimation, see ESI.1†). The ICP analysis reveals the presence of both metals in all samples (see Table 1).

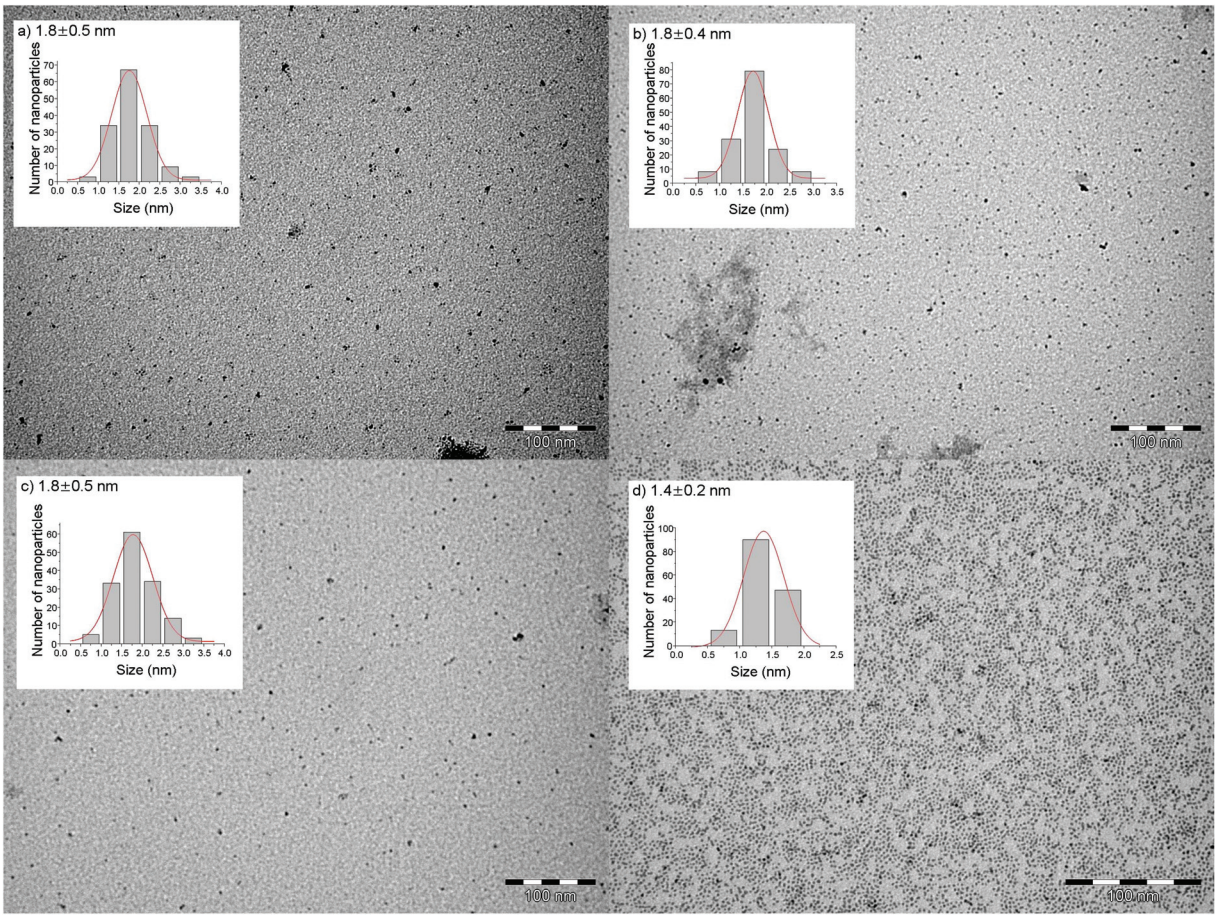

Fig. 1 TEM images with the corresponding size histograms of: (a) **Ru1Pt1**, (b) **Ru1Pt2**, (c) **Ru1Pt4** and (d) **Ru/PPP** NPs.

Table 1 Metal content and mean size of metal NPs

NP sample	% Ru[a]	% Pt[a]	Mean size[b] (nm)	Coherence length[c] (nm)
Ru1Pt1	23.1	37.1	1.8 (0.5)	2
Ru1Pt2	15.9	31.1	1.8 (0.4)	2.8
Ru1Pt4	8.6	75.3	1.8 (0.5)	3.5
Pt@Ru	18.0	40.0	2.0 (0.5)	—
Pt1Ru1	19.7	24.8	1.5 (0.3)	0.8
Pt1Ru2	35.5	19.5	1.4 (0.3)	1
Pt1Ru4	56.7	3.4	1.5 (0.4)	1
Ru/PPP	53.1	—	1.4 (0.2)	2
Pt/PPP	—	95.5	—[d]	>5
Pt/CO	—	82.1	1.4 (0.3)	—

[a] wt% by ICP. [b] Manual analysis of enlarged micrographs by measuring at least 150 NPs. [c] WAXS analysis. [d] Large and agglomerated nanoparticles (see ESI.2).

The TEM analyses of the second series of bimetallic nanoparticles (**Pt1Ru1**, **Pt1Ru2** and **Pt1Ru4**) show for all samples the presence of small NPs that are in some cases agglomerated (Fig. 2). The mean size distribution obtained from the TEM analyses reveals NPs of *ca.* 1.5 (0.3), 1.4 (0.3) and 1.5 (0.4) nm for **Pt1Ru1**, **Pt1Ru2** and **Pt1Ru4**, respectively (see Table 1). In that series, the increase of the NP mean size with respect to the first step (**Pt/CO** *ca.* 1.4 (0.3) nm) is less pronounced. There also, ICP analyses performed on purified NPs indicate the presence of both metals (see Table 1).

HRTEM was performed for the two series of NPs, evidencing crystalline NPs as shown in Fig. 3 and 4. The EDX (energy-dispersive X-ray spectroscopy) analyses were realised for a collection of particles or on individual particles, showing homogeneous composition in all of them and pointing out that the individual NPs are bimetallic. These analyses are in accordance with ICP analyses (Table 1 ESI.3†). Because of the HRTEM resolution, the crystalline structure pattern could be assigned more by analysing the displayed patterns – since hexagonal-close packed (hcp) and face-centred cubic (fcc) patterns strongly differ – rather than by determining the precise distances between the atomic planes. Indeed, the measured distances, between 0.21 and 0.24 nm, are consistent with both Pt (111) and Ru (100) planes. The **RuPt** series shows mainly the presence of particles displaying an fcc structure (Fig. 3 and Fig. 3–5 in ESI.3†) and the **PtRu** series shows mainly the presence of hcp structured nanoparticles (Fig. 4 and Fig. 6–8 ESI.3†).

The WAXS (wide angle X-ray scattering) studies provide pair distribution functions (PDFs) allowing both reciprocal and real space structural analysis of the series of colloids. The colloids **Ru1Pt1**, **Ru1Pt2** and **Ru1Pt4** are all well-crystallized (Fig. 5).

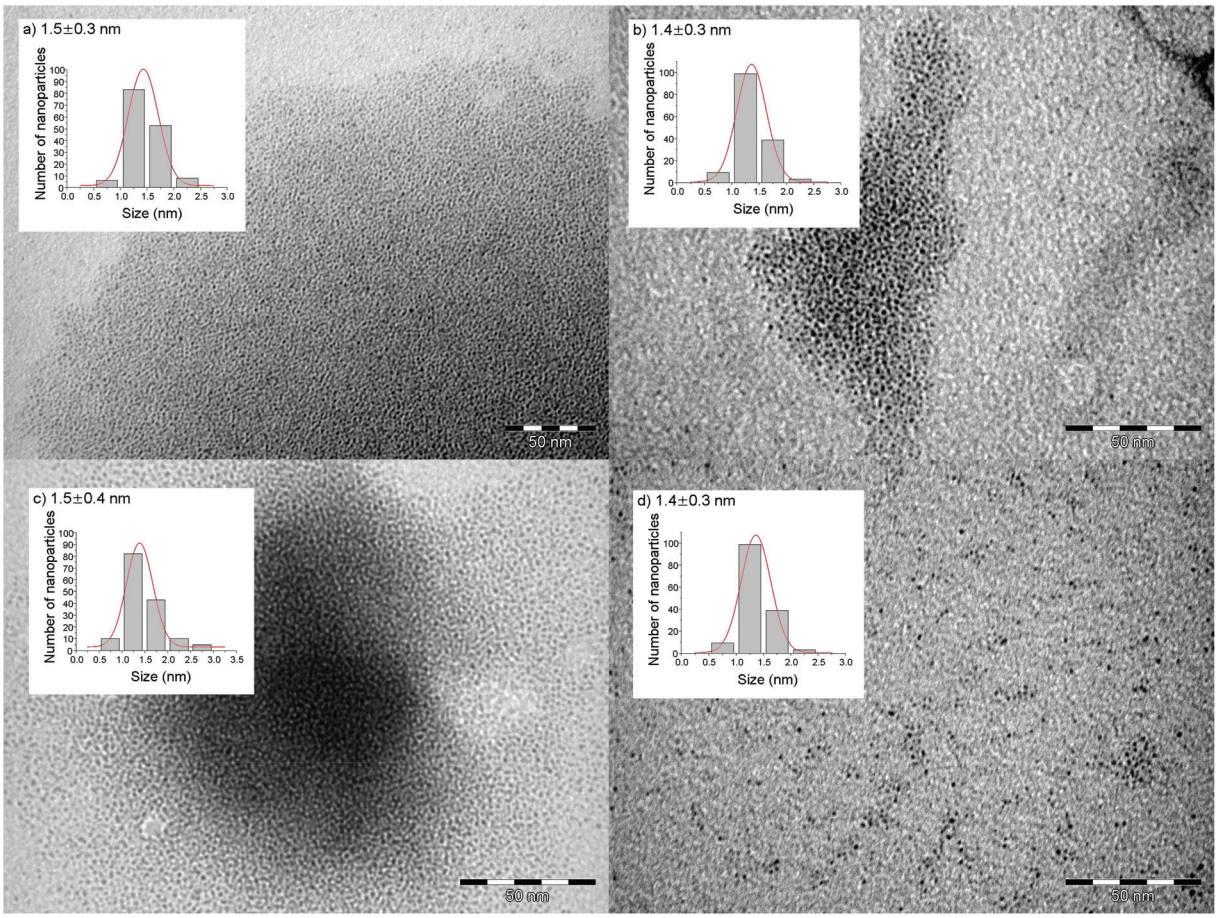

Fig. 2 TEM images with the corresponding size histograms of: (a) **Pt1Ru1**, (b) **Pt1Ru2**, (c) **Pt1Ru4** and (d) **Pt/CO** NPs.

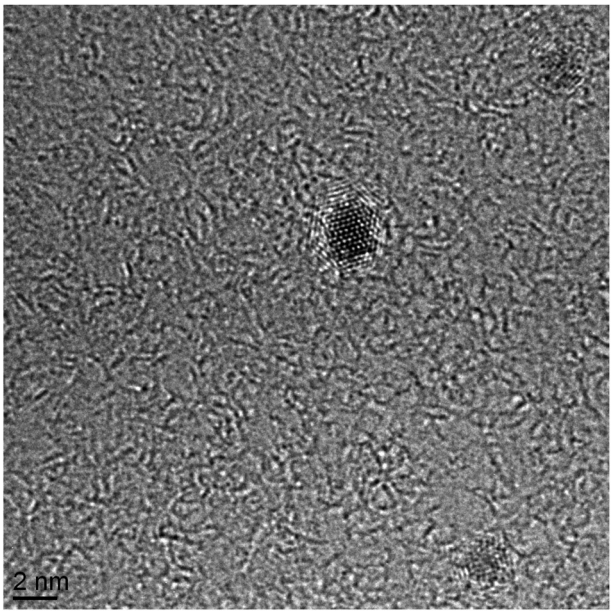

Fig. 3 HRTEM image of **Ru1Pt2** NPs.

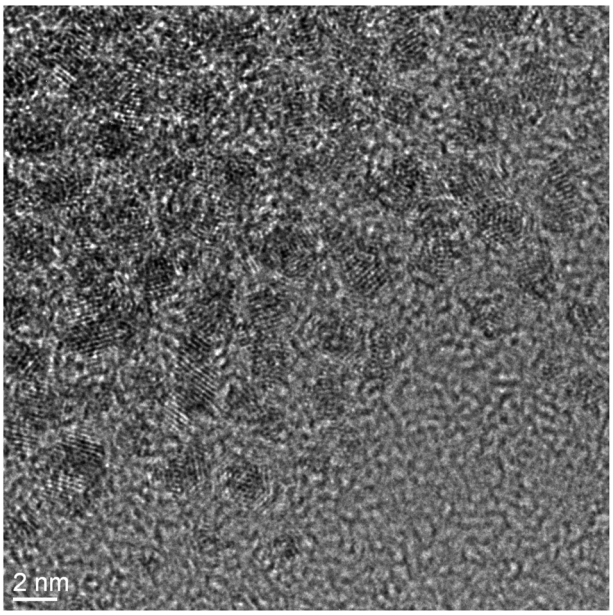

Fig. 4 HRTEM image of **Pt1Ru4** NPs.

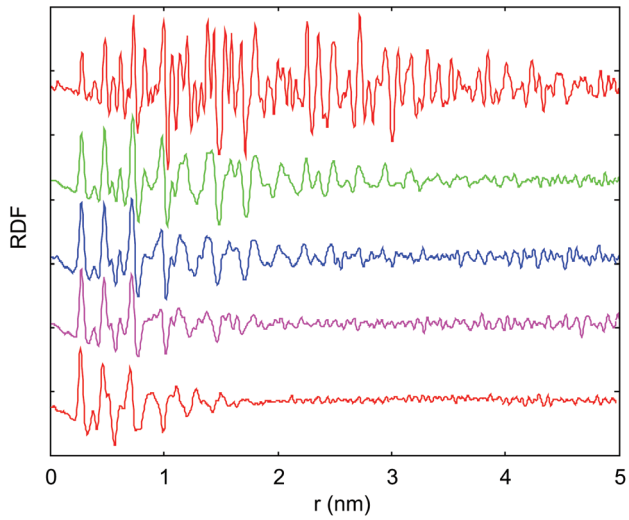

Fig. 5 WAXS analysis of bimetallic **RuPt** NPs (from top to bottom **Pt/PPP**, **Ru1Pt4**, **Ru1Pt2**, **Ru1Pt1**, and **Ru/PPP**).

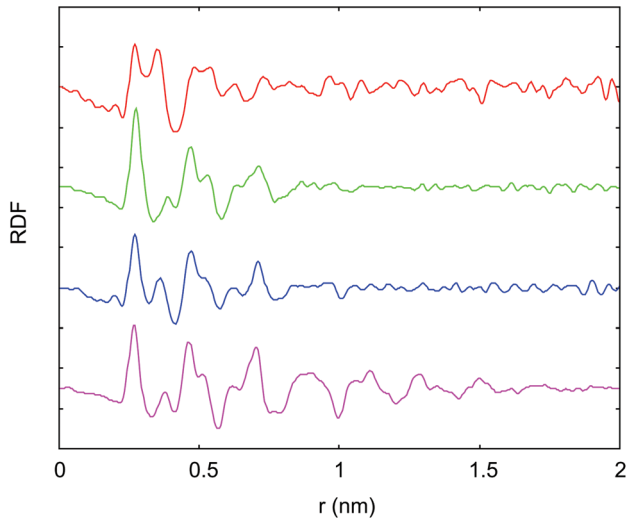

Fig. 6 WAXS analysis of bimetallic **PtRu** NPs (from top to bottom **Pt1Ru1**, **Pt1Ru2**, **Pt1Ru4** and **Ru/PPP**).

Their coherence lengths, which are measurements of the size of crystalline domains and are usually smaller than the true size except in the case of well-ordered single crystals, have been measured as 2.0 nm, 2.8 nm and 3.5 nm, respectively. These values are significantly larger than the sizes measured by TEM, probably due to the presence of some coalescence. For these three samples, the diffraction pattern is mostly fcc. Additionally, close inspection of the PDFs in the 0.8–1.1 nm range clearly indicates that a pattern typical of the fcc structure steadily increases from **Ru1Pt1** to **Ru1Pt4**, without significant change of the bond-length. This evolution, fully correlated with the one observed for correlation length and overall amplitude of the PDF, is consistent with a segregated system where Pt domains grow in size and generate a dominant Pt-like diffraction pattern. This result is consistent with DFT calculations on the formation mechanism of Pt(111) NP layers grown on the Ru(001) core.[28]

Observations are much different for the **PtRu** NPs (Fig. 6): for all of them, inspection in the reciprocal space reveals only very broad patterns and also a very strong peak at a very small angle (2–3° in 2theta). This points out to very small and poorly crystallized domains strongly interacting, *i.e.* fine scale agglomeration. Discrepancy between TEM sizes and coherence length is limited and actually fully consistent with the agglomeration of small domains in particles globally larger. Because

of the limited organization, limited information can be recovered. From the gradual evolution of the diffraction patterns in the reciprocal space, it appears that **Pt1Ru1** NPs are mostly hcp (small hcp peak at 25° and symmetry of main peak between 15° and 22°); fcc features can be observed combined with hcp ones for **Pt1Ru4**, **Pt1Ru2** being inversely strongly fcc but with hcp features. It should be emphasized that analysis in the reciprocal space strongly favours the best ordered domains, which clearly are limited in proportion for all **PtRu** samples.

Solid state infrared spectroscopy after reaction with CO

Since carbon monoxide is a sensitive probe for studying the surface composition of metal nanoparticles, the CO adsorption on the surface of the previously described NPs was investigated by attenuated total reflectance infrared spectroscopy (ATR-IR) in the solid state. In previous work, it has been shown by IR and NMR techniques that CO can be in dynamic exchange between terminal and bridging positions on the surface of Ru NPs, when only sterically stabilized with a polymer, namely polyvinylpyrrolidone (PVP). This exchange is prevented when dppb (1,4-bis(diphenylphosphino)butane) is used as the stabilizing ligand.[29] The surface chemistry of CO has been also investigated in ruthenium–platinum bimetallic NPs. The IR and NMR combined techniques help to identify the structure – alloy[16] or core–shell[17] – of RuPt bimetallic NPs stabilized by PVP prepared under different reaction conditions. In another work, probing the surface chemistry by adsorbing CO also helped to identify the chemical order of RuPt/dppb bimetallic NPs.[18] In this case, the NPs display a highly disordered structure with a ruthenium rich core surrounded by a shell containing both ruthenium and platinum.

Carbon monoxide was reacted with solid bimetallic or monometallic NPs in a Fisher-Porter bottle under mild conditions (1.5 bar of CO, r.t., 72 h). Then, ATR-IR spectra were recorded with a spectrometer available in a glove box. The obtained ATR-IR spectra of the **RuPt** series of bimetallic NPs together with the spectra of alloyed **Pt@Ru** and monometallic NPs **Ru/PPP** and **Pt/PPP** are depicted in Fig. 7. Fig. 8 presents the ATR-IR spectra of the **PtRu** series of bimetallic NPs and monometallic **Ru/PPP** and **Pt/CO** NPs. The **Ru/PPP** NPs display a CO band at 1970 cm^{-1}. This value is close to the CO band previously observed for Ru/dppb NPs.[18] For **Pt@Ru** NPs (Fig. 7-b) the CO band appears at 1999 cm^{-1}, a frequency which is in agreement with the presence of both Ru and Pt atoms on the surface of the bimetallic NPs as previously observed on the **RuPt/dppb** system.[18]

Concerning the **RuPt** series, we observed very broad signals of low intensity for the CO adsorption band as well as a red shift. The band shift and broadening increased with increasing platinum content, being the maximum with **Pt/PPP** NPs (Fig. 7-f)). **Ru1Pt1**, **Ru1Pt2** and **Ru1Pt4** samples show CO adsorption band similar to **Pt/PPP** nanoparticles, but different from the ones observed for RuPt bimetallic NPs previously prepared using the "chimie douce" approach (**RuPt/PVP**[17] or **RuPt/dppb**[18]). Albeit the structure of these bimetallic NPs

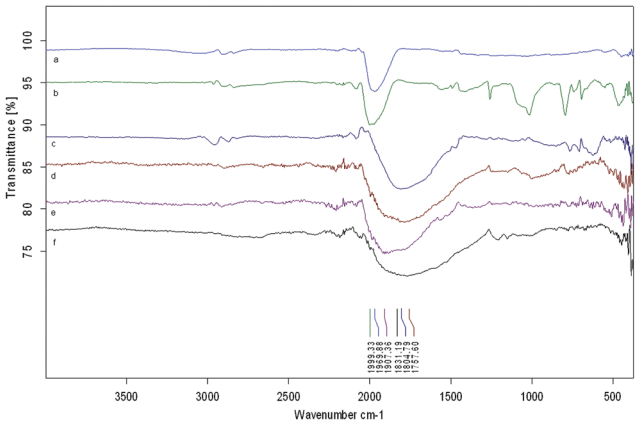

Fig. 7 ATR-IR spectra for **RuPt** NPs after CO exposure: (a) **Ru/PPP** (1970 cm^{-1}), (b) **Pt@Ru** (1999 cm^{-1}), (c) **Ru1Pt1**, (d) **Ru1Pt2**, (e) **Ru1Pt4**, and (f) **Pt/PPP**.

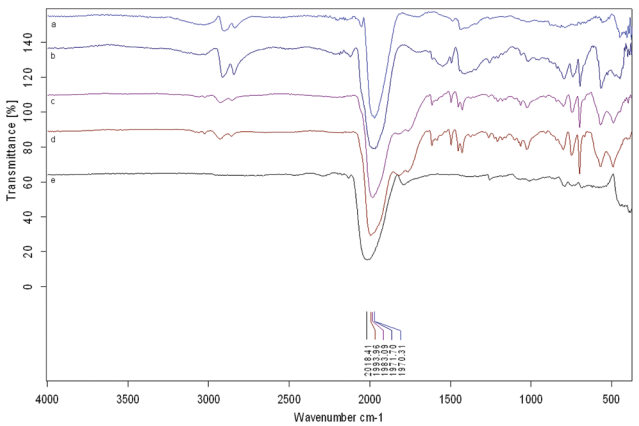

Fig. 8 ATR-IR spectra for **PtRu** NPs after CO exposure: (a) **Ru/PPP** (1970 cm^{-1}), (b) **Pt1Ru4** (1971 cm^{-1}), (c) **Pt1Ru2** (1983 cm^{-1}), (d) **Pt1Ru1** (1993 cm^{-1}), and (e) **Pt/CO** (2018 cm^{-1}).

cannot be clearly elucidated from these IR analyses, it seems that ruthenium atoms are not on the surface of the NPs for **Ru1Pt4** NPs, as the IR spectrum is similar to **Pt/PPP**. The intermediate spectra observed for **Ru1Pt1** and **Ru1Pt2** can indicate an intermediate covering of platinum on the NP surface. This behaviour can be due to several factors (as low CO coverage[30,31] or multiple individual bands, terminal or bridging[32]); however, further analyses are needed to shed some light on the surface chemistry of CO for these NPs, analyses that are beyond the scope of this work.

The CO adsorption at the surface of NPs for the **PtRu** series was also investigated by ATR-IR and compared to the monometallic **Ru/PPP** and **Pt/CO** NPs spectra (Fig. 8). In that case, all NPs show a narrow CO adsorption band. The band frequency increased with increasing platinum content following the order: **Ru/PPP** = **Pt1Ru4** < **Pt1Ru2** < **Pt1Ru1** < **Pt/CO**. The **Pt1Ru4** nanoparticles show a CO absorption band at the same frequency (1971 cm^{-1}) as the one observed for **Ru/PPP**

(1970 cm^{-1}), indicating that the surface of the **Pt1Ru4** NPs contains only ruthenium. The vibration frequencies observed for **Pt1Ru1** (1993 cm^{-1}) and **Pt1Ru2** (1983 cm^{-1}) are intermediate between that of **Pt/CO** NPs (2018 cm^{-1}) and that of **Ru/PPP** NPs (1970 cm^{-1}) indicating the presence of both metals on the NP surface.

From all the analyses presented above it seems reasonable to propose that a core–shell structure has been obtained at specific Ru : Pt ratio. From simple models we calculated that a ratio of 1 : 2 is needed to form a complete second metal monolayer. The **RuPt** NPs are well-crystallised, with an fcc character increasing with the Pt content. The amount of Pt on the surface of these particles increases with the Pt content. The **PtRu** particles are less crystallized, and present an important hcp character at high Ru loading and finally, the amount of Ru on the surface also increases with the Ru content. Taking into account the IR spectra after reaction with CO the **PtRu4** NPs are completely covered with ruthenium pointing out to a core–shell structure while the **PtRu1** and **PtRu2** nanoparticles seem to present a partially covered Pt core–Ru shell structure.

Catalysis

We evaluated the catalytic performances of the bimetallic NPs – and for comparative purposes the monometallic ones – for the selective hydrogenation of cinnamaldehyde (CAL) (Scheme 3). In this reaction, the formation of the saturated aldehyde (HCAL) is favoured over the unsaturated alcohol (COL) because of thermodynamics. The definition of selective catalysts for the production of COL is challenging. It has been shown that the product distribution depends on the structure and composition of NPs. The factors controlling the selectivity of the hydrogenation of α,β-unsaturated aldehydes are in general: the nature of the metal, the morphology of metal particles, the nature of the support and the presence of a second metal. It has been shown that unpromoted metals have specific selectivity towards unsaturated alcohols. The selectivity towards COL follows the series Ir > Pt > Ru > Rh > Pd. A dependence of selectivity on the metal particle size has been found for Pt, Rh, Ru and Co catalysts. Large nanoparticles are reported as more selective *versus* COL than smaller ones due to steric effect; the planar cinnamaldehyde molecule cannot adsorb parallel to a flat metal surface because of the repulsion of the aromatic ring, preventing the approach of the C=C bond to the surface, *i.e.* C=O bond is hydrogenated preferentially. The nature of the support plays also a role changing the electronic density of metal particles. In general, electron-donating species interacting with metal particles improve selectivity towards the saturated alcohol. This is due to the higher charge density on the metal surface which decreases the binding energy on the C=C bond favouring the hydrogenation of the C=O bond. Finally, the presence of a more electropositive metal in Pt NPs led to an increase towards the aldehyde hydrogenation. The second metal acts as an electron-donor ligand that increases the electron density on Pt, favouring C=O hydrogenation by decreasing the binging energy of the C=C bond. In the case of Pt-based bimetallic NPs the selectivity towards COL increases in the presence of iron, cobalt and ruthenium. This effect is attributed to an electrophilic activation of the C=O bond by electropositive metal atoms associated with platinum.[24–26]

The dependence of the selectivity on the structure and composition makes hydrogenation of unsaturated aldehydes as model reactions to establish relations between selectivity and catalyst structure. Thus, the analysis of the catalysis results can shed some light on the composition and the structure of the NPs described herein.

The catalytic results obtained at different reaction times are summarized in Table 2 for the **RuPt** series, Table 3 for the **PtRu** series and Table 4 for the monometallic NPs.

RuPt series

First, the activity of the **RuPt** NP series was compared to those of their corresponding monometallic counterparts (Tables 2 and 4). For the **RuPt** series the activity is increased at higher platinum content, following the tendency: **Ru1Pt4** > **Ru1Pt2** ≈**Ru1Pt1** > **Ru/PPP** ≈ **Pt/PPP** > **Pt@Ru** (see Fig. 9 for TON comparison). **Pt/PPP** showed a low activity, which can be explained by the much higher mean size of the particles leading to less active surfaces sites compared with smaller NPs. **Pt@Ru** NPs (Table 2, entries 13 to 16) show the lowest activity although the platinum content and the mean particle size are similar to those of **Ru1Pt2** NPs (Table 2, entries 5 to 8). This difference in activity should be the result of a difference in the chemical structure. **Ru1Pt2** were prepared through a two-step synthesis, leading to a higher platinum content on the surface (as estimated from the simple model applied, the reaction conditions used should lead to a complete Pt monolayer over Ru cores). The single-step procedure applied to synthesise **Pt@Ru** NPs should lead to a richer ruthenium surface than for **Ru1Pt2**, which could be responsible for the low activity observed. From the catalytic results we thus have an indirect evidence of the

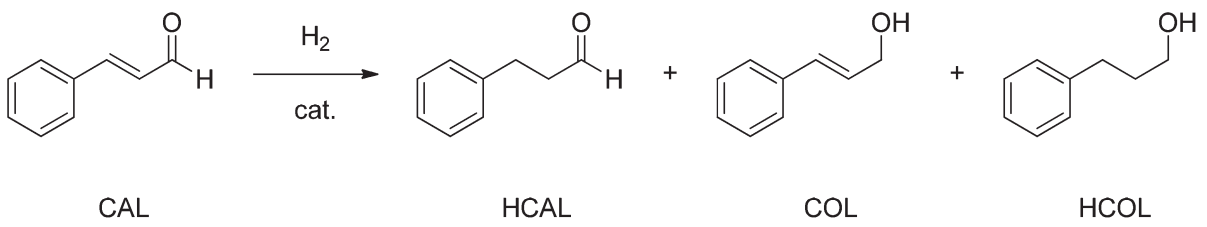

Scheme 3 *trans*-Cinnamaldehyde hydrogenation reaction.

Table 2 Cinnamaldehyde hydrogenation with bimetallic NPs **Ru1Pt1**, **Ru1Pt2**, **Ru1Pt4** and **Pt@Ru**

Entry	Catalysts	Time [h]	Conv. [%]	TON	TOF [h^{-1}]	HCAL [%]	HCOL [%]	COL [%]	Acetal [%]
1	**Ru1Pt1**	2	13	88	44	60	32	8	n.d.
2		4	27	190	47	49	29	22	n.d.
3		6	42	298.5	50	45	25	30	n.d.
4		22	64	449	20	27	28	41	4
5	**Ru1Pt2**	2	11	105	52	72	23	5	n.d.
6		4	18	172	43	68	25	7	n.d.
7		6	24	226	38	58	25	15	2
8		22	53	501	23	38	16	37	9
9	**Ru1Pt4**	2	25	163	81	76	12	13	n.d.
10		4	34	216	54	74	11	15	n.d.
11		6	44	282	47	68	13	18	1
12		22	87	556	25	51	26	22	1
13	**Pt@Ru**	2	5	40	20	79	8	13	n.d.
14		4	9	69	17	75	10	15	n.d.
15		6	14	111	18	77	8	15	n.d.
16		22	40	324	14	60	11	29	n.d.

Reaction conditions: 2.5 mg of bimetallic NPs, cinnamaldehyde (7.5 mmol), isopropanol (50 mL), P_{H_2} = 20 bar, T = 70 °C. Yields were determined by GC analysis using nonane (3.7 mmol) as an internal standard. n.d.: not detected.

Table 3 Cinnamaldehyde hydrogenation with bimetallic NPs **Pt1Ru1**, **Pt1Ru2** and **Pt1Ru4**

Entry	Catalysts	Time [h]	Conv. [%]	TON	TOF [h^{-1}]	HCAL [%]	HCOL [%]	COL [%]	Acetal [%]
1	**Pt1Ru1**	2	24	222	111	75	13	12	n.d.
2		4	29	271	68	65	14	19	2
3		6	34	314	52	57	15	25	3
4		22	82	763	35	30	23	33	14
5	**Pt1Ru2**	2	23	151	76	71	13	16	n.d.
6		4	43	283	71	71	12	16	1
7		6	45	300	50	66	13	19	2
8		22	80	527	24	38	24	30	8
9	**Pt1Ru4**	2	12	79	39	65	20	15	n.d.
10		4	14	94	23	59	19	22	n.d.
11		6	22	143	24	59	18	23	n.d.
12		22	53	348	16	38	21	40	1

Reaction conditions: 2.5 mg of bimetallic NPs, cinnamaldehyde (7.5 mmol), isopropanol (50 mL), P_{H_2} = 20 bar, T = 70 °C. Yields were determined by GC analysis using nonane (3.7 mmol) as an internal standard. n.d.: not detected.

Table 4 Cinnamaldehyde hydrogenation with monometallic NPs **Ru/PPP**, **Pt/PPP** and **Pt/CO**

Entry	Catalysts	Time [h]	Conv. [%]	TON	TOF [h^{-1}]	HCAL [%]	HCOL [%]	COL [%]	Acetal [%]
1	**Ru/PPP**	2	13	76	38	83	13	4	n.d.
2		4	18	105	26	75	12	13	n.d.
3		6	25	145	24	72	12	16	n.d.
4		22	71	409	19	58	20	21	1
5	**Pt/PPP**	2	15	89	44	75	15	10	n.d.
6		4	18	114	28	65	16	19	n.d.
7		6	27	163	27	54	18	26	2
8		22	63	386	18	38	24	28	10
9	**Pt/CO**	2	62	443	243	85	6	5	4
10		4	74	527	147	74	8	11	7
11		6	87	621	106	74	9	9	8
12		22	99	705	33	37	33	9	21

Reaction conditions: 2.5 mg of monometallic NPs, cinnamaldehyde (7.5 mmol), isopropanol (50 mL), P_{H_2} = 20 bar, T = 70 °C. Yields were determined by GC analysis using nonane (3.7 mmol) as an internal standard. n.d.: not detected.

structure of the metal NPs, indicating that the NPs synthesised in a two-step procedure have a richer platinum shell.

The comparison of the nanocatalyst selectivity towards the different hydrogenated products was performed at isoconversion (between 25 and 35% conv., see Fig. 10). The selectivity towards the carbon–carbon double bond hydrogenation (formation of HCAL) was high in all cases. The **RuPt** NP series showed that at higher platinum content the selectivity towards

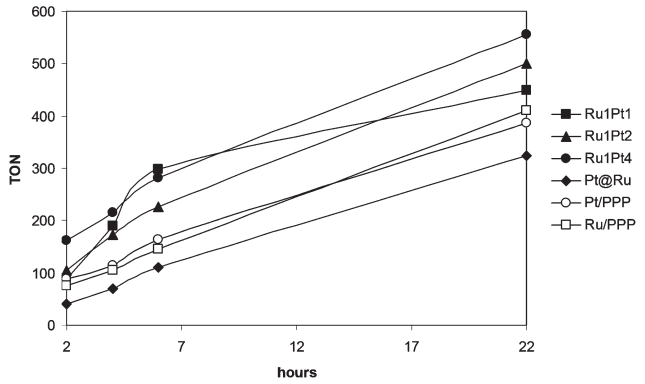

Fig. 9 Evolution of TON with time in the CAL hydrogenation using **RuPt** NPs.

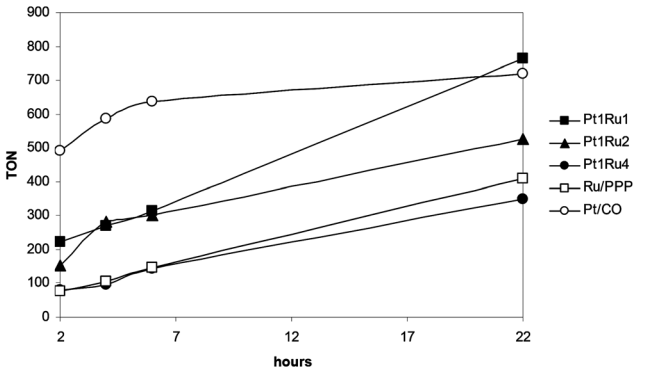

Fig. 11 Evolution of TON with time in the CAL hydrogenation using **PtRu** NPs.

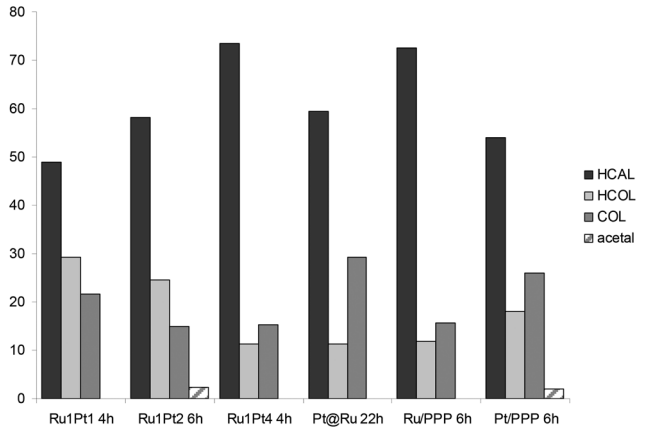

Fig. 10 Selectivity in *trans*-cinnamaldehyde hydrogenation for **RuPt** series.

HCAL increases, *i.e.* the increase of ruthenium content in the NPs leads, as expected, to a higher COL selectivity (up to 22% for **Ru1Pt1**). This indicates that Ru atoms are less available due to the formation of a Pt shell, and the positive effect on COL selectivity due to the presence of a second metal is no longer observed. The results also evidence a difference depending on the NP structure. The comparison of selectivity obtained for **Ru1Pt2** and **Pt@Ru** NPs (same metal composition with different structure) shows that, at similar conversion, **Pt@Ru** presents more affinity to C=O hydrogenation (29% COL) than **Ru1Pt2** (15%). Taking into account the core–shell structure of **Ru1Pt2**, ruthenium atoms are less available than in **Pt@Ru** (alloy structure), which are responsible for a high COL selectivity. On the other hand, **Pt/PPP** NPs showed the highest selectivity towards COL (up to 26%) which can be explained by the size of these NPs, as size-dependent selectivity has been previously observed.[24,33]

PtRu series

The activity of **PtRu** NPs was also compared to those of their corresponding monometallic counterparts (Tables 3 and 4 and Fig. 11 for TON comparison). As already observed for the **RuPt** series the activity is higher with increasing platinum content: **Pt/CO** ≫ **Pt1Ru1** > **Pt1Ru2** > **Pt1Ru4** ≈**Ru/PPP**. The **Pt/CO** catalyst is highly active, reaching a TOF of 243 h^{-1} after 2 h and 62% of conversion (Table 4, entry 9) in comparison with **Pt/PPP** (Table 4, entry 5, TOF of 44 h^{-1}). These different behaviours are attributed to the difference in particle size: indeed, as observed in TEM images, **Pt/CO** NPs are small and well-dispersed while **Pt/PPP** are large and agglomerated (ESI.2†). As is expected that smaller NPs are more active than larger ones, this explains the lower activity observed for **Pt/PPP** NPs. The catalytic results also seem to indicate that the two-step procedure led to a richer Ru surface, as the **Pt1Ru4** catalyst – as estimated, should contain almost two ruthenium layers – shows a similar activity as pure ruthenium NPs (see Fig. 11 for the TON evolution). Additionally, the catalytic results of a mixture of **Pt/CO** and **Ru/PPP** NPs (see ESI.4†) show that the activity is higher than those observed for the respective **PtRu** NPs. Indeed, in the **Pt/CO–Ru/PPP** nanoparticle mixture, the platinum surface is more accessible than in **PtRu** NPs – as Pt is covered by Ru – giving higher activities.

The comparison of the selectivity of **PtRu** NPs was performed at isoconversion (between 25 and 35% conv., see Fig. 12). The selectivity towards the carbon–carbon double bond hydrogenation was also high in all cases. The decrease of platinum content led to more selective catalysis towards COL (reaching 23% for **Pt1Ru4**). However, if we take into account that **Ru/PPP** and **Pt1Ru4** show comparable ("low") activity probably because of the high ruthenium content in **Pt1Ru4**, nevertheless we note that the small amount of platinum in these NPs leads to a higher COL selectivity (23% COL for **Pt1Ru4** *vs.* 16% COL for **Ru/PPP** at 6 h; Table 3, entry 11 and Table 4, entry 3). This tendency is observed until the end of the reaction (22 h) where the highest selectivity towards COL is reached (40% COL for **PtRu4** *vs.* 21% COL for **Ru/PPP**; Table 3, entry 12 and Table 4, entry 4), while maintaining relatively low total hydrogenation product (21% HCOL) and almost no acetal formation. Considering that these NPs have a core–shell structure (see above), this latter result suggests a synergistic effect between the Pt core and the Ru shell. Furthermore, the selectivity towards COL in the **Pt/CO–Ru/PPP** NP mixture (see ESI.4†)

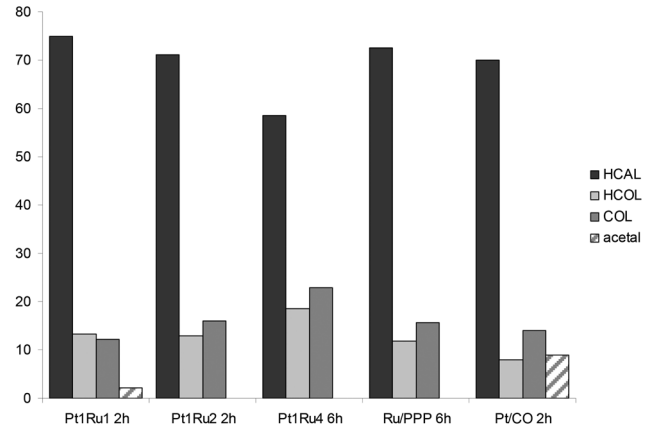

Fig. 12 Selectivity in *trans*-cinnamaldehyde hydrogenation for **PtRu** series.

is lower than in the respective **PtRu** NPs. This reveals that **PtRu** NPs are bimetallic and not a mixture of monometallic NPs, as the beneficial effect of a second metal is no longer observed. The comparison of the selectivity and activity at low conversions of the mixture of monometallic NPs with the bimetallic ones, together with the comparison of the activity of **Pt1Ru4** NPs with **Ru/PPP** NPs suggests again a core–shell structure for **PtRu** NPs.

TEM analyses of the NPs after catalysis were performed to check their stability under catalysis conditions. The TEM images (see ESI.5†) revealed that the mean size of the **RuPt** NPs increased after catalysis (see Table 5). Agglomerated and coalesced NPs are observed, particularly for **Ru1Pt4** (see ESI.5†), which are richer in platinum. The **Pt@Ru** NPs appeared to be more stable. On the other hand, **PtRu** NPs were also stable during hydrogenation as the nanoparticles display a similar mean size as before catalysis (see Table 5). Finally, the **Ru/PPP** and **Pt/CO** monometallic NPs were also stable under hydrogenation conditions as the mean size remained similar after catalysis. Surface platinum rich NPs (**RuPt** series) agglomerated and coalesced at the end of the reaction. For **Pt/PPP** NPs this behaviour was already observed during their synthesis since the monometallic **Pt/PPP** NPs are big and agglomerated (ESI.2†), pointing out that ruthenium surfaces are better stabilized by PPP than platinum NPs. On the other hand, it has been shown that PPP strongly interacts with the surface of ruthenium NPs through both arene rings by π-interaction.[21,22] Additionally, **PtRu** NPs have CO coordinated on their surface (see IR spectra on the ESI.6†), which gives an extra stabilization to the system with regard to the **RuPt** NPs.

Table 5 NP mean size before and after catalysis

	Mean size (nm) before catalysis[a]	Mean size (nm) after catalysis[a]
Ru1Pt1	1.8 (0.5)	4.4 (1.4)[b]
Ru1Pt2	1.8 (0.4)	2.4 (0.8)[b]
Ru1Pt4	1.8 (0.5)	2.9 (2)[b]
Pt@Ru	2.0 (0.5)	1.6 (0.4)
Pt1Ru1	1.5 (0.3)	1.4 (0.3)
Pt1Ru2	1.4 (0.3)	1.5 (0.2)
Pt1Ru4	1.5 (0.4)	1.5 (0.3)
Ru/PPP	1.4 (0.2)	1.5 (0.3)
Pt/PPP	>200[c]	>200[c]
Pt/CO	1.4 (0.3)	1.9 (0.6)

[a] Manual analysis of enlarged micrographs by measuring at least 150 nanoparticles. [b] Presence of agglomerates and coalesced NPs. [c] Estimation, big and agglomerated NPs.

Conclusions

Two different series of bimetallic NPs have been successfully prepared using a two-step procedure. To determine their structure they have been characterized by TEM, HRTEM and WAXS. The adsorption of carbon monoxide on the NP surface was also studied by ATR-IR. TEM and HRTEM show crystalline and monodisperse NPs and the EDX analyses reveal that the individual NPs are bimetallic. The WAXS analyses of the RuPt series indicate well-crystallized NPs with mostly fcc diffraction pattern. Additionally, the pattern typical of the fcc structure steadily increases from **Ru1Pt1** to **Ru1Pt4**, without significant change of the bond-length. For the PtRu series WAXS analyses show very small and poorly crystallized domains strongly interacting, *i.e.* fine scale agglomeration. The solid state infrared spectroscopy after reaction with CO clearly indicates for the PtRu series the increase of ruthenium content on the shell from **Pt1Ru1** to **Pt1Ru4**. However, we observed very broad signals of low intensity for the CO adsorption band in the RuPt series which are difficult to analyse. All these data allow us to conclude that the NPs display a core–shell type structure; nevertheless, deeper analyses, for example EXAFS study, are still needed to fully understand their precise structure.

The investigation of these nanoparticles as catalysts in the *trans*-cinnamaldehyde hydrogenation reaction not only led to interesting catalytic results but also gave complementary information about the structure of the NPs. Indeed, the activity and the selectivity observed are in agreement with a core–shell structure. As a general trend we have observed that the higher the surface platinum content, the higher the activity is. Thus the activity was higher for **Ru1Pt4** NPs in the RuPt series and for **Pt1Ru1** in the PtRu series. In addition the observation of different catalytic activities for alloy and core–shell NPs of the same metal content (**Ru1Pt2** and **Pt@Ru**) reveals that the seed-mediated synthesis led to the formation of core–shell NPs. The selectivity was also impacted by the composition and structure of the NPs. In the RuPt series the selectivity was higher when ruthenium and platinum atoms are both on the surface (partially covered core–shell NPs; **Ru1Pt1** and **Ru1Pt2** and alloyed **Pt@Ru** NPs). In the case of PtRu series, a synergistic effect on the selectivity between the metal of the core and the metal of the shell was observed.

As a general conclusion, besides the interest in the obtained results in catalysis, this work points out that selective catalysis can be a complementary tool to shed some light on

the structure and composition of metal nanoparticles, here helping on the characterization of few nanometer bimetallic NPs.

Experimental

General methods

All operations were carried out under an argon atmosphere using standard Schlenk techniques or in an MBraun glovebox. Solvents were purified by standard methods or by an MBraun SPS-800 solvent purification system. [Ru(COD)(COT)] and [$Pt(CH_3)_2$(COD)] were purchased from Nanomeps Toulouse, 4-(3-phenylpropyl)pyridine and *trans*-cinnamaldehyde from Sigma-Aldrich, and CO and H_2 from Air Liquid. All these reactants were used as received. **Pt@Ru**[9] and **Pt/CO**[27] NPs were prepared by previously described methods.

NPs were characterized by TEM and HRTEM after deposition of a drop of the crude colloidal solution on a covered holey copper grid. TEM and HRTEM analyses were performed at the "Service Commun de Microscopie Electronique de l'Université Paul Sabatier" (TEMSCAN-UPS): TEM by using a JEOL JEM 1011 CX-T electron microscope operating at 100 kV with a point resolution of 4.5 Å and HRTEM by using a JEOL JEM 2100F equipped with a Field Emission Gun (FEG) operating at 200 kV with a point resolution of 2.3 Å. The approximation of the particle mean size was made through a manual analysis of enlarged micrographs by measuring at least 150 particles on a given grid.

Wide-angle X-ray scattering (WAXS) was performed at CEMES-CNRS. Samples were sealed in 1 mm diameter Lindemann glass capillaries. The samples were irradiated with graphite-monochromatized molybdenum K_α (0.071069) radiation and the X-ray intensity scattered measurements were performed using a dedicated two-axis diffractometer. Radial distribution functions (RDF) were obtained after Fourier transformation of the reduced intensity functions.

ATR-IR spectra were recorded on a Perkin-Elmer GX2000 spectrometer available in a glovebox, in the range 4000–400 cm^{-1}.

ICP analyses were performed at the CNRS "Département Service Central d'Analyse Institut des Sciences Analytiques – UMR 5280" in Solaize.

Hydrogenation reactions were carried out in a Top Industrie stainless steel autoclave. Gas chromatographic analyses were run on a Perkin Elmer Autosystem XL equipped with a Restek Rtx 5-Amine column (30 m, 0.53 mm, 1 μm).

Synthesis of nanoparticles

RuPt nanoparticles. In a typical experiment the [Ru(COD)(COT)] complex was introduced into a Fisher-Porter reactor and dissolved with THF previously degassed by three freeze-pump cycles. The resulting yellow solution was cooled at −60 °C and a PPP/THF solution was added to the reactor. The reactor was pressurized with 3 bar of H_2 and the solution was left to reach slowly the room temperature. The solution, which turned black after 20 min of reaction, was kept under stirring overnight at r.t. After this period of time the Fisher-Porter bottle was depressurized and [$Pt(CH_3)_2$(COD)] was added to the black colloidal solution in the glovebox. A PPP/THF solution was introduced into the Fisher-Porter bottle at −60 °C. The reactor was pressurized with 3 bar of H_2 and the solution was heated at 70 °C for 30 min and then stirred at room temperature for 18 h. After this period of time, excess of H_2 was eliminated and the volume of solvent was reduced to 10 mL under vacuum. 40 mL of pentane were then added to the colloidal suspension, which was cooled down to −30 °C to precipitate the particles. After filtration under argon with a cannula, the black solid powder was washed twice with pentane (2 × 40 mL) and filtered again before drying under vacuum. For each Ru : Pt ratio studied, the quantities of reactants are detailed hereafter.

Ru1Pt1. 1st step: 142 mg (0.45 mmol) of [Ru(COD)(COT)]; 21.5 μL (0.12 mmol) of PPP and 90 mL of THF. 2nd step: 150 mg (0.45 mmol) of [$Pt(CH_3)_2$(COD)]; 21.5 μL (0.12 mmol) of PPP and 90 mL of THF. Yield: 92.2 mg. ICP analysis Ru: 23.1%, Pt: 37.1%.

Ru1Pt2. 1st step: 95 mg (0.3 mmol) of [Ru(COD)(COT)]; 14.4 μL (0.07 mmol) of PPP and 60 mL of THF. 2nd step: 200 mg (0.6 mmol) of [$Pt(CH_3)_2$(COD)]; 28.6 μL (0.15 mmol) of PPP and 120 mL of THF. Yield: 91.1 mg. ICP analysis Ru: 15.9%, Pt: 31.1%.

Ru1Pt4. 1st step: 57 mg (0.18 mmol) of [Ru(COD)(COT)]; 8.6 μL (0.04 mmol) of PPP and 36 mL of THF. 2nd step: 240 mg (0.72 mmol) of [$Pt(CH_3)_2$(COD)]; 34.4 μL (0.17 mmol) of PPP and 144 mL of THF. Yield: 123 mg. ICP analysis Ru: 8.6%, Pt: 75.3%.

PtRu nanoparticles. In a typical experiment the [$Pt_2(dba)_3$] complex was introduced into a Fisher-Porter reactor and dissolved with toluene previously degassed by three freeze–pump cycles. The reactor was pressurized with 1 bar of CO and the solution was stirred at room temperature for 1 h. The reactor was depressurized and the brown precipitate was filtered *via* a cannula and washed three times (3 × 40 mL) with toluene. The nanoparticles were dried under vacuum and then redispersed in THF. [Ru(COD)(COT)] was added to the suspension. A PPP/THF solution was introduced into the Fisher-Porter bottle at −60 °C. The reactor was pressurized with 3 bar of H_2 and stirred at room temperature overnight. After this period of time, the excess of H_2 was eliminated and the volume of solvent was reduced to 10 mL under vacuum. 40 mL of pentane were then added to the colloidal suspension, which was cooled down to −30 °C to precipitate the particles. After filtration under argon with a cannula, the black solid powder was washed twice with pentane (2 × 40 mL) and filtered again before drying under vacuum.

As previously, for each Pt : Ru ratio studied, the quantities of reactants are detailed hereafter.

Pt1Ru1. 1st step: 246 mg (0.45 mmol) of [$Pt_2(dba)_3$] and 60 mL of toluene. 2nd step: 142 mg (0.45 mmol) of [Ru(COD)(COT)]; 43 μL (0.22 mmol) of PPP and 180 mL of THF. Yield: 124.9 mg. ICP analysis Ru: 19.7%, Pt: 24.8%.

Pt1Ru2. 1st step: 164 mg (0.3 mmol) of $[Pt_2(dba)_3]$ and 40 mL of toluene. 2nd step: 187 mg (0.60 mmol) of [Ru(COD)(COT)]; 43 μL (0.22 mmol) of PPP and 180 mL of THF. Yield: 114.8 mg. ICP analysis Ru: 35.5%, Pt: 19.5%.

Pt1Ru4. 1st step: 98 mg (0.18 mmol) of $[Pt_2(dba)_3]$ and 24 mL of toluene. 2nd step: 227 mg (0.72 mmol) of [Ru(COD)(COT)]; 43 μL (0.22 mmol) of PPP and 180 mL of THF. Yield: 90.1 mg. ICP analysis Ru: 56.7%, Pt: 3.4%.

Ru/PPP. 284 mg (0.9 mmol) of the [Ru(COD)(COT)] complex were introduced into a Fisher-Porter reactor and dissolved with 80 mL of THF previously degassed by three freeze–pump cycles. The resulting yellow solution was cooled at −60 °C and a PPP/THF solution (43 μL (0.22 mmol) per 100 mL) was added to the reactor. The reactor was pressurized with 3 bar of H_2 and the solution was left to reach slowly the room temperature. The solution, which turned black after 20 min of reaction, was kept under stirring overnight at room temperature. After this period of time the Fisher-Porter bottle was depressurized and the volume of solvent was reduced to 10 mL under vacuum. 40 mL of pentane were then added to the colloidal suspension, which was cooled down to −30 °C to precipitate the particles. After filtration under argon with a cannula, the black solid powder was washed twice with pentane (2 × 40 mL) and filtered again before drying under vacuum. Yield: 88 mg. ICP analysis Ru: 53.1%.

Pt/PPP. 300 mg (0.9 mmol) of the $[Pt(CH_3)_2(COD)]$ complex were introduced into a Fisher-Porter reactor and dissolved with 80 mL of THF previously degassed by three freeze–pump cycles. The resulting solution was cooled at −60 °C and a PPP/THF solution (43 μL (0.22 mmol) per 100 mL) was added to the reactor. The reactor was pressurized with 3 bar of H_2 and the solution was heated at 70 °C for 30 min and then stirred at room temperature for 18 h. After this period of time, the excess of H_2 was eliminated and the volume of solvent was reduced to 10 mL under vacuum. 40 mL of pentane were then added to the colloidal suspension which was cooled down to −30 °C to precipitate the particles. After filtration under argon with a cannula, the black solid powder was washed twice with pentane (2 × 40 mL) and filtered again before drying under vacuum. Yield: 78 mg. ICP analysis Pt: 95.5%.

Surface reactivity with CO

The adsorption of carbon monoxide on the surface of metal NPs was performed in the solid state as follows. A purified sample of nanoparticles was introduced into a Fisher-Porter bottle. The reactor was pressurized with 1.5 bar of CO for 72 h. Then, the CO gas was evacuated under vacuum for 20 min and the ATR-IR spectra were recorded.

Catalysis

In a typical experiment, the autoclave was purged by three vacuum/argon cycles. The suspension formed from the corresponding NPs (2.5 mg), *trans*-cinnamaldehyde (7.5 mmol) and nonane (3.7 mmol) in isopropanol (50 mL) was introduced into the autoclave. The autoclave was pressurized with 20 bar of H_2 and heated to 70 °C. After the desired reaction time, the autoclave was cooled to room temperature and depressurised. The reaction mixture was then analysed by gas chromatography.

Acknowledgements

This work was supported by the Centre National de la Recherche Scientifique (CNRS), which we gratefully acknowledge. We thank the Chinese Scholarship Council (CSC) for the X. Q. grant. V. Collière (LCC and UPS-TEMSCAN) and L. Datas (UPS-TEMSCAN) are also acknowledged for TEM/HRTEM facilities.

References

1 *Nanomaterials in Catalysis*, ed. P. Serp and K. Philippot, Wiley, 2013.
2 F. Tao, *Chem. Soc. Rev.*, 2012, **41**, 7977–7979.
3 B. Wu, D. Hu, Y. Kuang, B. Liu, X. Zhang and J. Chen, *Angew. Chem., Int. Ed.*, 2009, **48**, 4751–4754.
4 H. Liu, C. Song, L. Zhang, J. Zhang, H. Wang and D. P. Wilkinson, *J. Power Sources*, 2006, **155**, 95–110.
5 E. Antolini, *J. Power Sources*, 2007, **170**, 1–12.
6 S. Alayoglu, A. U. Nilekar, M. Mavrikakis and B. Eichhorn, *Nat. Mater.*, 2008, **7**, 333–338.
7 J.-Y. Ruzicka, D. P. Anderson, S. Gaw and V. B. Golovko, *Aust. J. Chem.*, 2012, **65**, 1420–1425.
8 E. Castillejos, M. Jahjah, I. Favier, A. Orejon, C. Pradel, E. Teuma, A. M. Masdeu-Bulto, P. Serp and M. Gomez, *ChemCatChem*, 2012, **4**, 118–122.
9 E. Castillejos, P.-J. Debouttière, L. Roiban, A. Solhy, V. Martinez, Y. Kihn, O. Ersen, K. Philippot, B. Chaudret and P. Serp, *Angew. Chem., Int. Ed.*, 2009, **48**, 2529–2533.
10 S. Alayoglu, P. Zavalij, B. Eichhorn, Q. Wang, A. I. Frenkel and P. Chupas, *ACS Nano*, 2009, **3**, 3127–3137.
11 J. Meurig Thomas, R. D. Adams, E. M. Boswell, B. Captain, H. Gronbeck and R. Raja, *Faraday Discuss.*, 2008, **138**, 301–315.
12 B. Chaudret and K. Philippot, in *Comprehensive Organometallic Chemistry III*, Editors-in-Chief, ed. H. C. Robert and D. M. P. Mingos, Elsevier, Oxford, 2007; pp. 71–99.
13 C. Amiens, B. Chaudret, D. Ciuculescu-Pradines, V. Colliere, K. Fajerwerg, P. Fau, M. Kahn, A. Maisonnat, K. Soulantica and K. Philippot, *New J. Chem.*, 2013, **37**, 3374–3401.
14 B. Chaudret, *C. R. Phys.*, 2005, **6**, 117–131.
15 D. Ciuculescu, C. Amiens, M. Respaud, A. Falqui, P. Lecante, R. E. Benfield, L. Jiang, K. Fauth and B. Chaudret, *Chem. Mater.*, 2007, **19**, 4624–4626.
16 C. Pan, F. Dassenoy, M.-J. Casanove, K. Philippot, C. Amiens, P. Lecante, A. Mosset and B. Chaudret, *J. Phys. Chem. B*, 1999, **103**, 10098–10101.

17 P. Lara, M.-J. Casanove, P. Lecante, P.-F. Fazzini, K. Philippot and B. Chaudret, *J. Mater. Chem.*, 2012, **22**, 3578–3584.
18 P. Lara, T. Ayval, M.-J. Casanove, P. Lecante, A. Mayoral, P.-F. Fazzini, K. Philippot and B. Chaudret, *Dalton Trans.*, 2013, **42**, 372–382.
19 L. Rodríguez-Pérez, C. Pradel, P. Serp, M. Gómez and E. Teuma, *ChemCatChem*, 2011, **3**, 749–754.
20 E. J. García-Suárez, M. Tristany, A. B. García, V. Collière and K. Philippot, *Microporous Mesoporous Mater.*, 2012, **153**, 155–162.
21 I. Favier, S. Massou, E. Teuma, K. Philippot, B. Chaudret and M. Gómez, *Chem. Commun.*, 2008, 3296–3298.
22 I. Favier, P. Lavedan, S. Massou, E. Teuma, K. Philippot, B. Chaudret and M. Gomez, *Top. Catal.*, 2013, **56**, 1253–1261.
23 M. Jahjah, Y. Kihn, E. Teuma and M. Gómez, *J. Mol. Catal. A: Chem.*, 2010, **332**, 106–112.
24 P. Gallezot and D. Richard, *Catal. Rev. Sci. Eng.*, 1998, **40**, 81–126.
25 P. Claus, *Top. Catal.*, 1998, **5**, 51–62.
26 P. Mäki-Arvela, J. Hájek, T. Salmi and D. Y. Murzin, *Appl. Catal., A*, 2005, **292**, 1–49.
27 A. Rodriguez, C. Amiens, B. Chaudret, M.-J. Casanove, P. Lecante and J. S. Bradley, *Chem. Mater.*, 1996, **8**, 1978–1986.
28 H.-L. Chou, F.-J. Lai, W.-N. Su, K. C. Pillai, L. S. Sarma and B.-J. Hwang, *Langmuir*, 2011, **27**, 1131–1135.
29 F. Novio, K. Philippot and B. Chaudret, *Catal. Lett.*, 2010, **140**, 1–7.
30 A. M. Bradshaw and F. M. Hoffmann, *Surf. Sci.*, 1978, **72**, 513–535.
31 R. P. Eischens and W. A. Pliskin, in *Adv. Catal.*, ed. D. D. Eley, W. G. Frankenburg, V. I. Komarewsky and P. B. Weisz, Academic Press, 1958, vol. 10, pp. 1–56.
32 A. Duteil, R. Queau, B. Chaudret, R. Mazel, C. Roucau and J. S. Bradley, *Chem. Mater.*, 1993, **5**, 341–347.
33 J. Teddy, A. Falqui, A. Corrias, D. Carta, P. Lecante, I. Gerber and P. Serp, *J. Catal.*, 2011, **278**, 59–70.